ENSO-Like Variability: 1900–2013*

Xianyao Chen

Key Laboratory of Physical Oceanography, Ocean University of China, Qingdao, China

John M. Wallace

Department of Atmospheric Sciences, University of Washington, Seattle, Washington

(Manuscript received 4 May 2015, in final form 24 August 2015)

ABSTRACT

ENSO-like variability is examined using a set of univariate indices based on unfiltered monthly global sea surface temperature (SST), sea level pressure (SLP), outgoing longwave radiation (OLR), sea level, and the three-dimensional ocean temperature (OT) fields. These indices, many of which correspond to the leading principal components (PCs) of the respective global fields, are highly correlated with each other. In combination with their spatial regression patterns, they provide a comprehensive description of ENSO-like variability in the atmosphere and ocean across time scales ranging from months to decades, from 1950 onward. The SLP and SST indices are highly correlated with one another back to the late nineteenth century. The interdecadal-scale shifts in the prevailing polarity of ENSO that occurred in the 1940s, the 1970s, and around the year 2000 are clearly evident in low-pass-filtered time series of these indices.

On the basis of empirical mode decomposition, ENSO-like variability is partitioned into an interannual "ENSO cycle," to which equatorial ocean wave dynamics imparts a distinctive equatorial signature, and a red noise background continuum, most prominent on the interdecadal time scale, which resembles the ENSO-like variability in some models in which the atmosphere is coupled to a slab ocean. The background continuum bears the imprint of the Pacific–North American (PNA) pattern, the leading mode of the Northern Hemisphere wintertime variability of the atmospheric circulation over the Pacific sector. The superposition of the ENSO cycle and the background continuum imparts a distinctive frequency dependence to the patterns of ENSO-like climate variability.

1. Introduction

The prominence of El Niño–Southern Oscillation (ENSO) among the patterns of climate variability is due to the existence of the so-called "Bjerknes feedback" mechanism, which involves the interplay between the strength of the trade winds and sea surface temperature (SST) anomalies in the equatorial cold tongue in the eastern Pacific (Bjerknes 1969, 1972; Rasmusson and Carpenter 1982). The signature of ENSO is reflected in the remarkably strong observed temporal correlations between indices of the Southern Oscillation in the sea level pressure field and indices of tropical Pacific SST anomalies.

Transitions between the contrasting ENSO polarities— El Niño (weak trade winds, warm SST) versus La Niña (strong trade winds, cold SST)—can come about in two ways: they may arise through zonally propagating oceanic Kelvin and Rossby waves that develop and propagate zonally in the equatorial thermocline in response to the time-varying wind forcing and function as a "delayed oscillator" (Cane and Zebiak 1985; Zebiak and Cane 1987; Battisti and Hirst 1989) or, alternatively, they may be stochastically forced, through the action of anomalous energy fluxes at the atmosphere–ocean inter face that project upon the optimal initial structure that is

conducive to the growth of ENSO-like SST anomalies (Penland and Sardeshmukh 1995; Newman 2007). There is evidence that the relative importance of these mechanisms is frequency dependent. For example, in statistics derived from a numerical experiment with a coupled model, Vimont et al. (2002) found that the delayed oscillator mechanism is operative on the interannual time scale but on the interdecadal time scale they found little evidence of delayed signals reflecting off the western boundary.

Pronounced swings in the Southern Oscillation coupled with ENSO-like tropical SST anomalies can occur even in the absence of ocean planetary wave propagation on the equatorial thermocline. In long integrations of global climate models in which the ocean is represented by a passive mixed layer "slab," whose temperature at each grid point varies in response to the net energy flux at the air–sea interface, the leading mode of variability is ENSO-like (Kitoh et al. 1999; Dommenget and Latif 2008; Dommenget 2010). Clement et al. (2011) compared results from a series of experiments in which the same atmospheric model was coupled to two different ocean models: one with a realistic representation of equatorial wave dynamics and the other with a slab ocean. ENSO-like variability was prominent in both, but the associated frequency spectra (shown in their Fig. 4) were quite different. The former exhibited a pronounced spectral peak on interannual time scales while the latter spectrum was red, with a predominance of interdecadal variability.

Early observational studies of ENSO were focused on the interannual variability associated with the cycling back and forth between short-lived El Niño and La Niña episodes. The occurrence of a pronounced "regime shift" in the climate system from the prevalence of the cold (strong trade wind) state of ENSO toward the prevalence of the warm (weak trade wind) state around 1976, as documented by Nitta and Yamada (1989), Trenberth (1990), Trenberth and Hurrell (1994), and Graham (1994), was instrumental in raising awareness of "ENSO-like interdecadal variability."

By applying 6-yr high-pass and low-pass filters to the principal components of the SST field, Zhang et al. (1997, hereinafter ZWB) partitioned ENSO-like variability into an "ENSO cycle–related" component on the interannual time scale, and what they referred to "residual ENSO-like variability," mainly on the interdecadal time scale. They showed that the interannual and interdecadal components exhibit somewhat different spatial signatures in the global SST, sea level pressure (SLP), and wind stress fields. The SST anomalies are less equatorially confined in the eastern Pacific and are relatively more prominent over the extratropical

North Pacific in the interdecadal component than in the interannual "ENSO cycle" component. These distinctions are clearly discernible in the observations but they are not strong enough to render the interannual and interdecadal components spatially orthogonal.

Garreaud and Battisti (1999) extended the analysis of ZWB to include a more detailed representation of the Southern Hemisphere circulation and demonstrated the remarkable equatorial symmetry of interdecadal ENSO-like variability. Based on the analysis of a set of climate indices derived from instrumental and tree ring records, Minobe (1997) showed evidence of regime shifts of alternating polarity in the Pacific sector around 1890, in the 1920s, in the 1940s, and in 1976/77, which he interpreted as manifestations of a 50–70-yr climate oscillation over the North Pacific.

In a study of North Pacific interdecadal climate variability and its effects on North American salmon production, Mantua et al. (1997) coined the term Pacific decadal oscillation (PDO), whose state is represented by the amplitude and polarity of the leading principal component of sea surface temperature field (strictly speaking, the departure from global mean sea surface temperature) over the North Pacific poleward of 20°N. Folland et al. (1999) introduced the term interdecadal Pacific oscillation (IPO), defined as the third EOF of the 13-yr low-pass-filtered global SST field. The spatial pattern of the IPO resembles the ENSO-like variability documented by ZWB and, by construction; its time-varying index emphasizes the interdecadal variability. Indices of the PDO and the IPO are widely used for representing ENSO-like interdecadal variability.

In this paper we update, augment, and refocus the analysis in ZWB with a view toward distinguishing between variability that involves ocean mixed layer dynamics and that which can be understood on the basis of interactions between the atmosphere and a slab ocean. The period of record is extended by 20 years (1994–2013), which includes the recent interval of anomalously strong trade winds and relatively low SST in the eastern equatorial Pacific cold tongue region. We augment the analysis in ZWB by including sea level data based on satellite altimetry and tide gauges, as well as gridded subsurface ocean temperature data and outgoing longwave radiation (OLR).

The paper is structured as follows. In the next section we describe the data sources and analysis techniques. In section 3, we describe the analysis of the SST, OLR, SLP, sea level, and three-dimensional ocean temperature (OT) fields, respectively, based on unfiltered monthly mean data. The analysis involves consideration of the leading EOFs of each of these fields in a global domain and their respective principal component (PC)

time series. We use PC1 of the SST departure field (referred to as our ENSO index or EI) as a reference time series for interrelating ENSO-like variability in the various fields. In section 4, we consider the frequency dependence of ENSO-like variability. In the final section we summarize and interpret what we consider to be our most important findings.

2. Data and analysis techniques

The analysis of the paper is based on following datasets:

- SST anomalies from updated version of Extended Reconstructed Sea Surface Temperature (ERSST.v3b) analysis from the NOAA/Climate Prediction Center;
- global SLP data from the Twentieth Century Reanalysis (20CR; Compo et al. 2011) obtained from the Physical Division of NOAA/Environmental Science Research Laboratory (ESRL);
- interpolated OLR data (1979–2013) as described in Liebmann and Smith (1996);
- objectively analyzed subsurface temperature and salinity at 24 levels in the upper 1500 m during 1950–2012 (version 6.13) provided by Ishii and Kimoto (2009);
- global sea surface height (SSH) based on satellite altimetry from the Archiving, Validation, and Interpretation of Satellite Oceanographic Data (AVISO); and
- tide gauge records from the Permanent Service of Mean Sea Level.

We also make use of the Southern Oscillation index (SOI), defined as standardized difference between Tahiti and Darwin standardized SLP anomalies (Tahiti minus Darwin) available at http://www.cgd.ucar.edu/cas/catalog/climind/soi.html.

In performing EOF analysis upon the SST, steric sea level (SSL), and SSH fields, we make use of unfiltered monthly departure fields (SST*, SSL*, and SSH*), defined at each grid point as the departures of local anomalies from the concurrent global-mean field; for example, SST* = SST − [SST], where [·] denotes the global average of the anomaly field (relative to a fixed reference climatology) for the same month. The same approach was used in ZWB. The notion of an SST departure field is implicit in the definitions of the cold tongue index (CTI) (Deser and Wallace 1990) and the Atlantic multidecadal oscillation (Trenberth and Shea 2006). The analysis of OLR and SLP is based on anomalies that have not had the global mean removed. In forming the data matrix for EOF analysis, the datum at each grid point is weighted in proportion to the

square root of cosine of latitude so that the variance at each grid point is weighted in proportion to the area of the grid box. Missing data points are set equal to their climatological values. The expansion coefficient time series derived from EOF analysis, referred to as the principal components, are all standardized to unit variance. EOF patterns are generated by regressing the various monthly fields upon their respective PC time series. The amplitudes that appear on EOF maps derived in this manner are representative of typical amplitudes of the ENSO-related excursions in that variable.

In documenting the frequency dependence of ENSO-like variability we use, as a reference amplitude, the amplitude of the SST anomalies in the equatorial Pacific cold tongue region; that is, we express the regression coefficients in units of dimensional amplitude per degree Celsius of SST anomalies in the cold tongue region. This ratio is obtained by dividing the regression coefficient per standard deviation of the reference time series by the regression coefficient of the unfiltered cold tongue index upon the same reference time series. For a formal definition of the CTI, see section 3a.

In displaying time series and in computing correlation coefficients we make use of a centered 5-month running mean smoothing operator to reduce high-frequency variability, much of which is related to the Madden–Julian oscillation. However, unless otherwise noted, the regression analyses and EOF analyses from which the various ENSO indices are derived are all based on unfiltered monthly mean data.

Names, acronyms, brief definitions, and references for the various ENSO indices referred to in this paper are listed in Table 1.

3. Results based on unfiltered data

In this section we show regression maps and time series documenting ENSO-like variability in sea surface temperature (section 3a), outgoing longwave radiation (section 3b), sea level pressure (section 3c), sea level (section 3d), and ocean temperature (section 3e), all on the basis of unfiltered monthly mean data. The results presented in sections 3a and 3c are a review and updating of results that first appeared in ZWB but for the other variables the results presented here are new.

a. Sea surface temperature

Niño-3.4 and the equatorial Pacific cold tongue index are widely used to categorize the status of ENSO. Both indices are based on areal averages of monthly mean SST anomalies over prescribed boxes centered in the

TABLE 1. Acronyms and names of the ENSO-like indices referred to in this study together with brief definitions and references where applicable.

Acronym	Full name
EI	ENSO index. PC1 of global SST*
EEI	Extratropical ENSO index. PC1 of Pacific SST poleward of 20°N/S
DEI	Decadal ENSO index. 12-yr low-pass-filtered EI
DEEI	Decadal extratropical ENSO index. 12-yr low-pass-filtered EEI
CTI	Cold tongue SST* index (Deser and Wallace 1990)
Niño-3.4	Cold tongue SST index (Rasmusson and Carpenter 1982; Trenberth and Hoar 1997)
SOI	Conventional Southern Oscillation index (Troup 1965; Trenberth and Shea 1987)
SOI*	Alternative SOI based on tropical marine data (ZWB)
IPO	Interdecadal Pacific oscillation (Folland et al. 1999)
PDO	Pacific decadal oscillation. PC1 of Pacific SST poleward of 20°N (Mantua et al. 1997)
SPDO	Southern Hemisphere PDO. PC1 of Pacific SST poleward of 20°S

equatorial Pacific: 5°S–5°N, 120°–170°W for Niño-3.4 versus 6°S–6°N, 180°–90°W for the CTI (Fig. 1a). Niño-3.4 is a measure of equatorial Pacific SST, whereas the CTI is a measure of the SST departure from global-mean SST, as explained in the previous section. This adjustment has very little effect on the interannual variability of the CTI, but on longer time scales it serves to cancel out the global warming signal. By construction, the difference curve (Fig. 1b) closely parallels the global-mean SST time series.

When EOF analysis is performed upon the raw global SST field "mode mixing" may occur between the ENSO-like variability and the global warming

signal; that is, ENSO-like features and the secular global warming trend may appear together in the same modes [e.g., as in Figs. 1 and 2 of Zhang et al. (2010)]. To circumvent this problem, we perform EOF analysis on the SST* field, as explained in the previous section. The leading EOF (hereafter EOF1) is shown in Fig. 2a and its expansion coefficient or, as it is often called, principal component time series (PC1) is shown in Fig. 2d. We will also refer to PC1 of the unfiltered, monthly mean, global SST* field as our ENSO index (see also Table 1, top row). EOF1 of SST* for the Pacific domain is shown in Fig. 2b and its PC time series in Fig. 2d. That the global and Pacific EOFs and their corresponding PC time series are virtually identical demonstrates that ENSO is, for all practical purposes, a Pacific phenomenon.

In EOF1 of global SST* shown in Fig. 2a, the largest amplitudes are observed in the equatorial Pacific cold tongue region, with weaker secondary features at subtropical and extratropical latitudes. To demonstrate that the pattern of ENSO-like variability in SST* really extends into the extratropics we performed EOF analysis on the SST* field poleward of 20°N/S in the Pacific domain, designated as P–TP. Figure 2c shows the leading EOF. The corresponding PC, which we will also refer to as the extratropical ENSO index (EEI), corresponds to the bottom time series in Fig. 2d. Apart from slight differences and amplitude, the subtropical and extratropical features in Figs. 2b and 2c are very similar and the corresponding PC time series (EI and EEI) are highly correlated ($r = 0.86$ based on 5-month running mean data). Consistent with results presented in ZWB, the interdecadal variability is slightly more prominent in EEI.
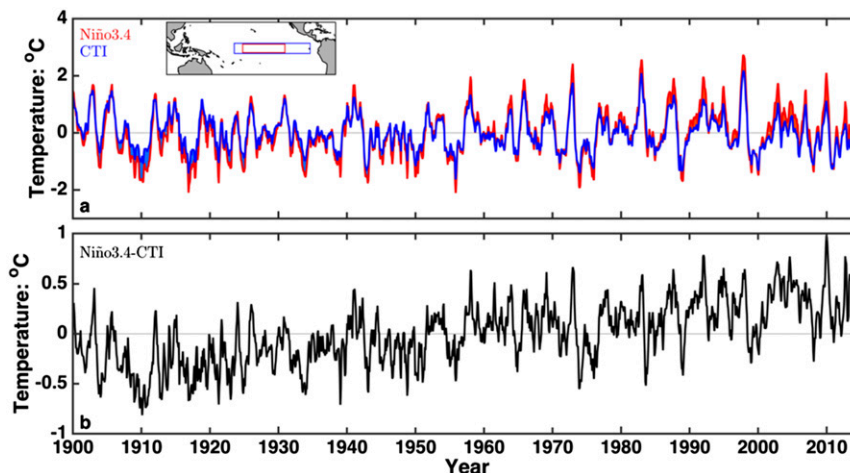

FIG. 1. (a) Time series of Niño-3.4 (red) and the cold tongue index (CTI) (blue) during 1900–2013 derived from the ERSST.v3b dataset, and (b) the difference between them (the black time series). The inset in (a) shows the regions over which SST is averaged in the respective indices.
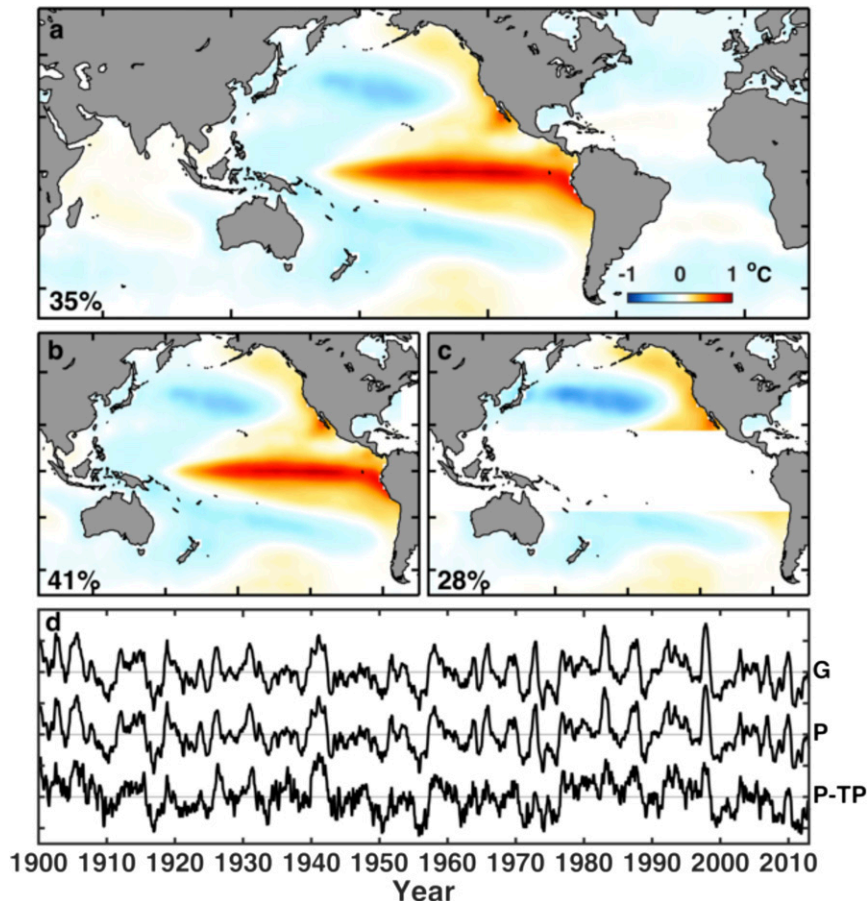
FIG. 2. EOF1 of SST* over (a) the global ocean (G), (b) the Pacific (P), and (c) the Pacific excluding the tropical Pacific (P–TP; i.e., 20°S–20°N) based on data for 1900–2013. EOFs are scaled in units of degrees Celsius per unit amplitude of the corresponding standardized PC time series. Percentages printed in the lower left corners refer to explained variance of the global SST* field. (d) The corresponding respective standardized PCs, as labeled. The interval between tick marks on the vertical axis is 2.0 standard deviations, which is same in the following figures unless otherwise specified. Henceforth G will be referred to as our El Niño index EI and P–TP as our extratropical ENSO index EEI.

b. Outgoing longwave radiation

It has been known almost back to the time when OLR observations first became available that the leading EOF is closely associated with ENSO-like variability (Heddinghaus and Krueger 1981; Rasmusson and Carpenter 1982). The leading EOF of OLR in the tropical domain 30°S–30°N for the 35-yr period of record 1979–2013, shown in Fig. 3a, is virtually identical to the pattern obtained by regressing OLR upon the EI (Fig. 3b). During El Niño years the Pacific intertropical and subtropical convergence zones encroach on the equatorial dry zone, particularly in the equatorial region near the date line, while the Maritime Continent is anomalously dry. The 5-month running mean time series of PC1 of OLR and the EI, shown in Fig. 3d, are correlated at a level of $r = 0.92$.

c. Sea level pressure

EOF analysis of the unfiltered monthly global SLP field does not yield a robust leading mode that encapsulates the ENSO-like variability in the historical record. Hence, in this section we will rely exclusively on empirically derived ENSO indices based on the SLP field, the most widely used of which is the Southern Oscillation index, defined in Trenberth and Shea (1987) as the standardized difference between the standardized SLP anomalies at Darwin and Tahiti. ZWB defined an alternative Southern Oscillation index (SOI*): standardized, area-averaged SLP over the tropical (20°N–20°S) Pacific sector east of the date line minus standardized area-averaged SLP over the remainder of the tropical oceans. The analysis is performed upon two different SLP datasets: ICOADS and 20CR, for which
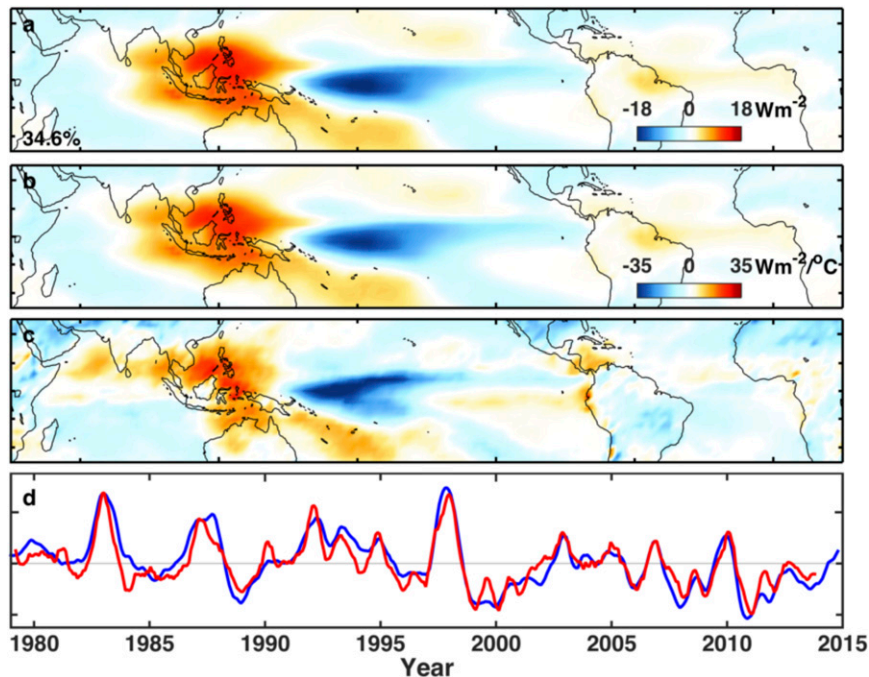
FIG. 3. (a) EOF1 of unfiltered monthly OLR, scaled as in Fig. 2. The percentage refers to the explained variance of OLR. Also shown are the regression patterns constructed by projecting the OLR onto (b) unfiltered and (c) 12-yr Lanczos low-pass-filtered PC1 of the OLR over the tropical domain (30°S–30°N), expressed in units of watts per meter squared per degree Celsius of the CTI. (d) Unfiltered, standardized PC1 of OLR (red) and the EI (blue).

the results are very similar back to about 1940. In the text we show results based on 20CR only. Corresponding results based on the ICOADS dataset are presented in Figs. S1–S3 in the supplementary material.

Time series of the EI, SOI, and SOI* are shown in Fig. 4. Consistent with results of ZWB, SOI* is more strongly coupled with the EI than the conventional SOI ($r = -0.90$ vs -0.82 from 1900 through 2013; see also Table 3). Accordingly, henceforth in this paper we will use SOI* as our primary Southern Oscillation index.

Correlation and regression patterns for SLP based on SOI* are shown in the top panels of Fig. 5. The correlations are strongest in the tropical belt and they conform closely to the boxes used in the definition of SOI*. The extratropical features are more prominent in the regression pattern, which gives a better indication of the amplitude of the ENSO-like variability in the extratropical wind field. In El Niño years (EI+), the SLP anomalies are of the polarity indicated in Fig. 5, with an anomalously weak west–east SLP gradient across the equatorial Pacific, and anomalously weak trade winds.

ZWB analyzed not only SLP but also the vectorial field of surface wind stress based on COADS. Their results offer guidance for relating SLP and surface wind stress. Along the equator the surface wind stress tends to be

zonally oriented and proportional to the east–west SLP gradient. When SLP is anomalously high in the eastern Pacific and low over the Maritime Continent, the westward wind stress in the central Pacific is anomalously strong. In the Northern and Southern Hemisphere subtropical trade wind belts the anomalous wind stress can be qualitatively inferred from the anomalous SLP gradient, making use of the geostrophic relationship.

d. Sea level

Variations in the field of global sea level have been monitored by satellite altimetry since 1993. They can be inferred indirectly over a longer time span from subsurface measurements of temperature and salinity. Here we refer to the former as sea surface height and the latter as steric sea level. At low latitudes SSL is mainly a reflection of changes in subsurface temperature and in estimating it we use temperature data only.

Lombard et al. (2005) showed that EOF1 of global SSL is dominated by ENSO-like variability, and that EOF1 of SSL over the North Pacific domain is strongly correlated with the PDO index. When EOF analysis is performed on short records of SSH or SSL [e.g., as in Nerem et al. (1997)], the leading mode that emerges appears to be a combination of ENSO-related,
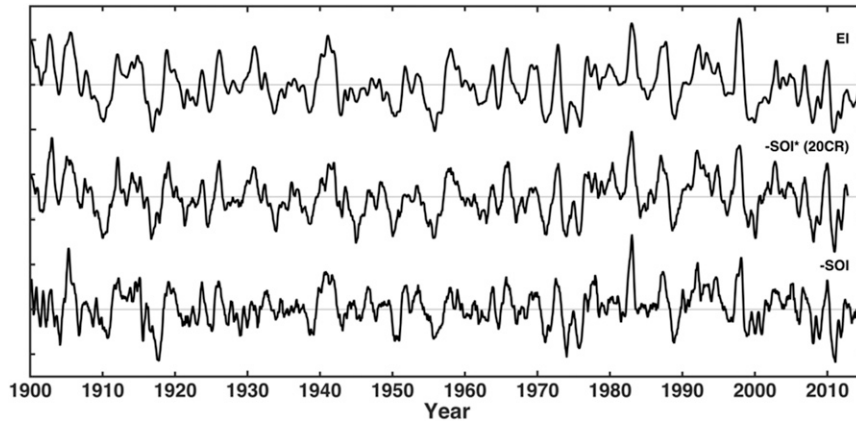
FIG. 4. The EI, defined as PC1 of the global, unfiltered SST* field (top time series); the alternative Southern Oscillation index SOI* defined as tropical (20°S–20°N) SLP (middle time series; the partial zonal mean from the date line to the South American coast minus the mean over the remainder of the tropics, based on 20CR); and the conventional (Darwin minus Tahiti) Southern Oscillation index (SOI; bottom time series).

dynamically induced sea level trends and human-induced sea level rise. To eliminate the possibility of such mode mixing, we performed EOF analysis on the departure fields SSH* and SSL*, as opposed to the raw fields.

The leading EOFs of global SSL* (Fig. 6a) and SST* (Fig. 2a) exhibit similar structures with primary centers of action over the central and eastern equatorial Pacific. In SSL* the anomalies of opposing polarity are concentrated over the tropical western Pacific, whereas in SST* they extend into middle latitudes. Based on data for 1950–2012, PC1 of SSL* and PC1 of SST* (the EI) are correlated at a level of $r = 0.89$ and the correlations are even stronger in more recent years, when the subsurface thermal data are more complete (e.g., $r = 0.93$ for 1970–2013).

For the overlapping period of record 1993–2012, shown in Fig. 6b, the PC1 of SSL* and SSH* are almost identical

($r = 0.98$), and the same is true of the corresponding regression patterns (not shown). By construction, the common downward trend in these time series has no relation to variations in global-mean sea level rise: it reflects the dynamical response of SSH and SSL to the strengthening of the trade winds during this period. Downward trends in the EI and SOI* from 1998 to 2013 are also clearly apparent in Fig. 4.

ENSO-like variability in sea level is also well captured in 100+-yr-long tide gauge (TG) records for San Francisco and Fremantle, which are representative of the eastern and western poles of the Pacific dipole pattern, as shown in in Fig. 6a. The monthly TG difference time series San Francisco minus Fremantle is shown in Fig. 6d together with the EI. From 1950 onward the correlation between the two time series is $r = 0.84$. It is notable that the variability of ENSO can be represented so well with just two
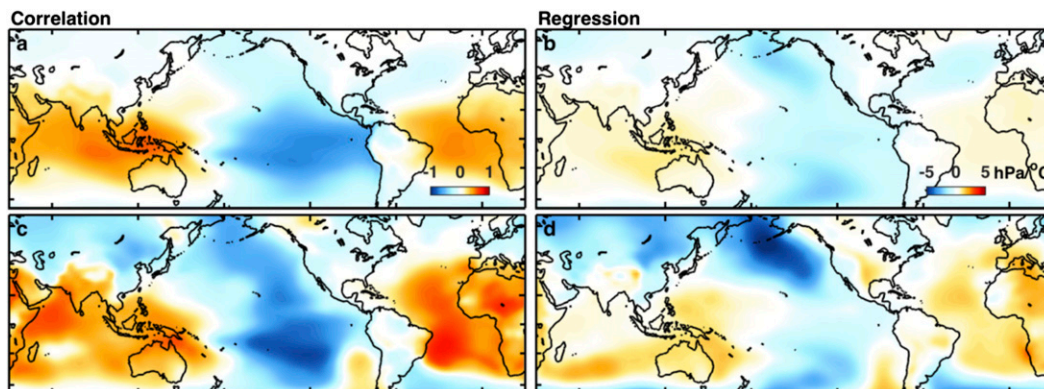

FIG. 5. (left) Correlation coefficients and (right) regression coefficients for the global SLP field based on (a),(b) the unfiltered SOI* and (c),(d) the 12-yr low-pass-filtered SOI*. Regression coefficients are expressed in units of hectopascals per degree Celsius of the CTI.
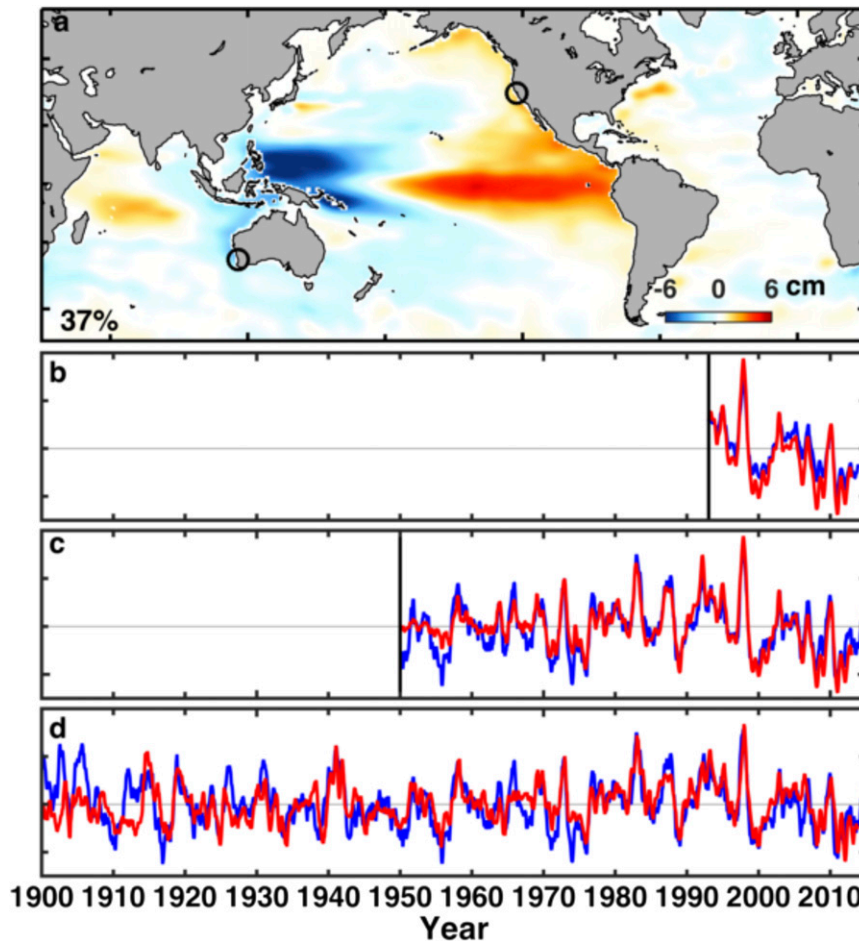
FIG. 6. (a) EOF1 of global steric sea level (SSL) based on data for 1950–2012 expressed in units of centimeters per standard deviation of its PC time series. Circles indicate the locations of the San Francisco and Fremantle tide gauge stations. The percentage refers to the explained variance of the global SSL* field. (b) Standardized PC of the leading mode of global steric sea level (SSL*, red line) and the leading PC of the global total sea level (SSH*, blue line) obtained from satellite altimetry, 1993–2012. (c) As in (b), but for SSL* (red) and the EI (blue), based on data for 1950–2012. (d) San Francisco minus Fremantle tide gauge record (red) and the EI (blue). Tick marks on the y axes in (b)–(d) are at intervals of two standard deviations.

tide gauge stations situated in the outer reaches of its dipole pattern in sea level.

e. Ocean temperature

To explore the three-dimensional structure of the subsurface ENSO-like variability we also analyzed the ocean temperature (OT) data level by level. For this purpose we performed EOF analysis on the mass-weighted Ishii and Kimoto (2009) subsurface temperature data in a global domain with 2.5° latitude × 2.5° longitude resolution and uneven vertical grid spacing, with highest resolution near the surface. Regression patterns for PC1, which accounts for 33% of the variance in that three-dimensional global domain, are shown in Fig. 7. The horizontal structure of vertically

integrated (700 m up to the surface) OT and the PC1 time series are nearly identical to their counterparts for steric sea level shown in previous figures ($r = 0.98$ for the PC time series). The PC time series is also strongly correlated with the EI ($r = 0.85$). In agreement with results of Roemmich and Gilson (2011), the subsurface temperature variations on the equator, shown in Fig. 7b, are strongest along the sloping Pacific thermocline. The node near 160°W separates the shallower anomalies on the eastern side of the basin from the deeper anomalies on the western side. The anomalies in the east (Fig. 7d) are narrowly focused on the equator, suggestive of a Kelvin wave signature, while the deeper anomalies to the west (Fig. 7c) exhibit separate centers along 12°N and 6°S, suggestive of an equatorial Rossby wave.
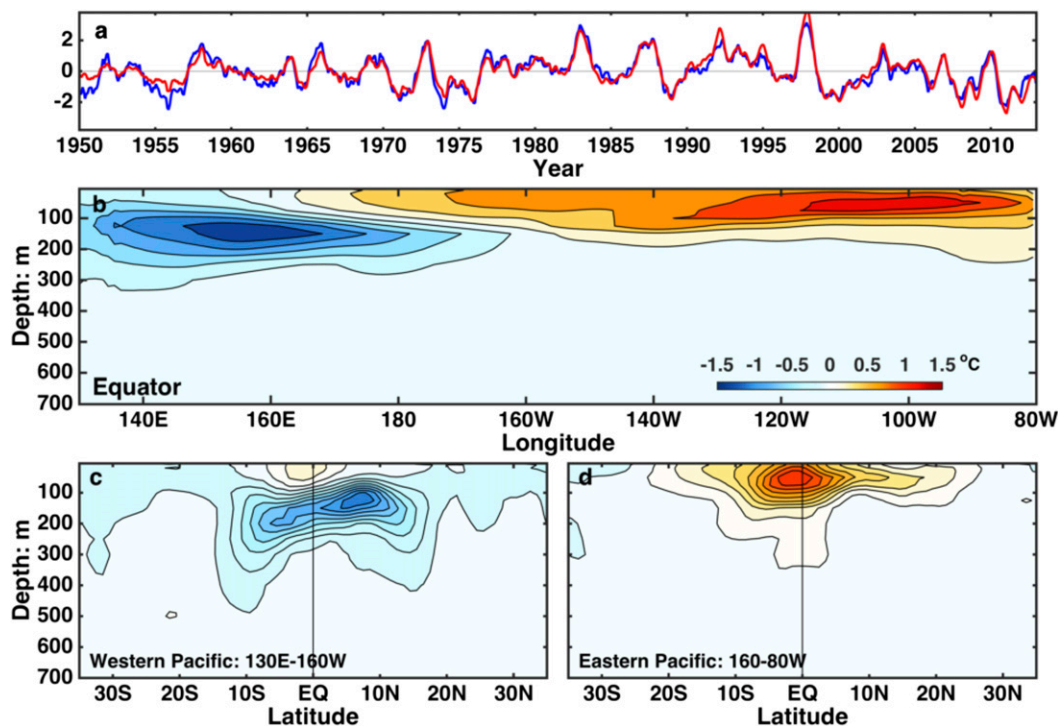
FIG. 7. (a) The EI (blue) and the PC1 of the three-dimensional ocean temperature (OT) field down to 700-m depth based on data for 1950–2012 (red). (b) Longitude–depth section of EOF1 of global OT on the equator. Also shown is zonally averaged OT in EOF1 of global OT in the (c) western Pacific sector (130°E–160°W) and (d) eastern Pacific sector (160°E–80°W). EOFs are scaled as in Fig. 2.

Similar patterns have appeared in numerical simulations of ENSO (e.g., Fig. 14 of Lau et al. 1992).

Figure 8 shows EOF1s of the three-dimensional fields of OT*, performed separately on an upper layer extending from 75 m upward to the ocean surface and a lower layer at 75–700 m. These modes account for 47% and 33% of the variances in their respective layers and their PC time series are correlated with one another at a level of $r = -0.89$. EOF1 of the upper layer closely resembles EOF1 of SST*: its PC is correlated with the EI at a level of $r = 0.95$. EOF1 of the lower layer is dominated by off-equatorial Rossby wave–like features in the far western Pacific. Neither of these patterns, like the full OT* signature in the previous figure or the SSL* pattern shown in Fig. 6a, exhibits strong planetary-scale signatures in the Atlantic basin or in the Southern Ocean. The subsurface signature of ENSO-like variability is largely restricted to the Pacific sector and the west coast of Australia.

f. Synthesis

Time series of the EI, the EEI, and the SOI* extending back in time to 1870 are shown in Fig. S1. Coherent ups and downs associated with interannual ENSO-like variability first start to become clearly discernible in multiple indices during the 1880s.

Many of the key findings of this section are summarized in Tables 2 and 3, which show correlation coefficients between all possible pairs of univariate indices of ENSO-like variability during 1900–2012 and 1950–2012, respectively. In addition to PC1 of SST* for the domain P–TP (i.e., the EEI), it includes separate Northern and Southern Hemisphere extratropical Pacific PC1 time series: the former is equivalent to the definition of the PDO and the latter in some sense its mirror image. Correlations range as high as 0.90 for some of the indices and most of them are stronger in the data from 1950 onward, presumably because of the improved data reliability. Monthly values of EI, EEI, SOI*, SOI, and TG are presented in the supplemental material.

4. Frequency dependence of ENSO-like variability

Using PC1 of unfiltered global SST* (i.e., EI) as a reference time series, we now investigate the frequency dependence of the ENSO-related variability.
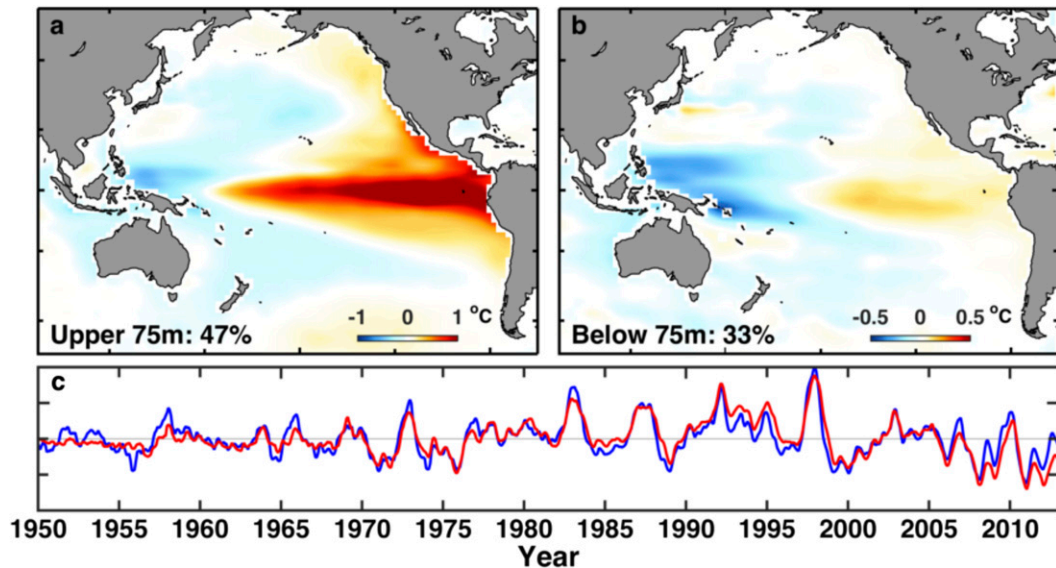
FIG. 8. EOF1 of vertically integrated OT* in (a) the uppermost 75 m and (b) the layer from 75 to 700 m, scaled as in Fig. 2. (c) The corresponding PC time series, blue for the upper layer and red for lower layer.

a. SST*

Performing empirical mode decomposition (EMD; Huang et al. 1998) upon the EI yields nine nearly orthogonal intrinsic mode functions (IMFs), whose sum is identical to the EI itself. By construction, the individual IMFs, shown in Fig. 9a, exhibit preferred mean time scales of 4 months (IMF 1), 8 months (IMF 2), 18 months (IMF 3), 3 years (IMF 4), 6 years (IMF 5), 12 years (IMF 6), 24 years (IMF 7), and 100 years or longer (IMFs 8 and 9). In Fig. 9b, we show sums of IMFs 1–4 and IMFs 5–9. The former can be viewed as a high-pass filtered time series and the latter as low-pass-filtered time series of the EI with cutoff periods of ~4–5 years. Bearing in mind that each IMF in the spectrum of an idealized white noise time series explains half as much variance as the preceding IMF (Wu and Huang 2004), the variance spectrum of IMFs 1–4 in Fig. 9a exhibits a 2–4-yr spectral peak, while the sum of IMFs 5–9 exhibits a red noise continuum that transitions to red noise on the multidecadal time scales and longer, as shown in Fig. 10. The red noise continuum resembles the simulated spectrum shown in Fig. 4 of Clement et al. (2011) from their simulation in which their atmospheric model was coupled with a slab ocean model, and the spectral peak is like the one obtained when the same atmospheric model was coupled to an ocean model with equatorial dynamics.

To explore the frequency dependence of the structure of ENSO-like variability in SST* we show in Fig. 11 the spatial patterns obtained by regressing the unfiltered monthly SST* field upon these IMFs. The

pattern based on the sum of IMFs 1–4 exhibits a distinctive equatorial signature, whereas the one based on the sum of IMFs 5–9 exhibits a more diffuse spatial signature biased toward the North Pacific. Qualitatively similar diffuse signals are obtained for summations of IMFs 5 and 6–9, shown in Fig. S4 in the supplementary material. The results are likewise insensitive to whether IMFs 1 and 2 are grouped with 3 and 4 (not shown).

Many published studies of ENSO-like interdecadal variability are based on data that have been low-pass filtered with a cutoff frequency of about one cycle per 12 years. The widely used interdecadal Pacific oscillation, defined in the introduction, is based on 13-yr

TABLE 2. Correlation matrix for ENSO indices: 1900–2012. EI is PC1 of SST*. EEI is PC1 of SST* poleward of 20°N/S in the Pacific domain and the subscripted NH and SH refer to the Northern and Southern Hemisphere subdomains. SOI* is the Southern Oscillation index defined as tropical (20°S–20°N) SLP: the partial zonal mean from the date line to the South American coast minus the mean over the remainder of the tropics, based on 20CR. SOI is the Darwin minus Tahiti station-based Southern Oscillation index. TG is the difference between the tide gauge records of the San Francisco and Fremantle. All correlations based on 5-month running means.

	EI	EEI	$(EEI)_{NH}$	$(EEI)_{SH}$	SOI*	SOI
EI	—					
EEI	0.86	—				
$(EEI)_{NH}$	0.71	0.94	—			
$(EEI)_{SH}$	0.82	0.79	0.54	—		
SOI*	−0.90	−0.72	−0.59	−0.70	—	
SOI	−0.82	−0.65	−0.50	−0.69	0.80	—
TG	0.69	0.57	0.50	0.48	−0.67	−0.66

TABLE 3. Correlation matrix for ENSO indices: 1950–2012. Besides the time series shown in Table 2, SSL* and OT* are PC1s of the SSL and the OT departure fields, respectively. Upper_75 and lower_75 denote the mean OT departure fields from ocean surface to 75-m depth and the lower layer of 75–700 m, respectively. OLR is the PC1 of the outgoing longwave radiation during 1979–2012. SSH* is the PC1 of the SSH departure field during 1993–2012.

	EI	EEI	$(EEI)_{NH}$	$(EEI)_{SH}$	SOI*	SOI	TG	SSL*	OT*	Upper_75	Lower_75	OLR
EI	—											
EEI	0.86	—										
$(EEI)_{NH}$	0.73	0.95	—									
$(EEI)_{SH}$	0.84	0.81	0.59	—								
SOI*	−0.92	−0.75	−0.62	−0.76	—							
SOI	−0.89	−0.72	−0.57	−0.78	0.90	—						
TG	0.84	0.74	0.65	0.68	−0.79	−0.78	—					
SSL*	0.89	0.74	0.60	0.76	−0.84	−0.82	0.84	—				
OT*	0.85	0.76	0.63	0.77	−0.79	−0.78	0.82	0.98	—			
Upper_75	0.95	0.76	0.63	0.76	−0.92	−0.87	0.84	0.94	0.90	—		
Lower_75	−0.84	−0.76	−0.65	−0.73	0.80	0.77	−0.83	−0.95	−0.97	−0.89	—	
OLR	0.92	0.76	0.61	0.82	−0.91	−0.91	0.84	0.95	0.92	0.95	−0.91	—
SSH*	0.93	0.89	0.80	0.81	−0.815	−0.87	0.91	0.98	0.97	0.93	−0.96	0.92

low-pass-filtered data. The Pacific decadal oscillation is generated from unfiltered data but often smoothed to focus on the interdecadal variability. In Fig. 12 time series of those indices are compared with a 12-yr low-pass Lanczos filtered time series of the EI. For convenience, we will refer to this smoothed version of the EI as the decadal ENSO index (DEI). The chronologies of the three indices are very similar, especially from 1940 onward. All three time series exhibit features suggestive of regime shifts in the 1920s, 1940s, 1970s, and around 2000.

Regression patterns for the DEI, the IPO, and the PDO shown in Fig. 13 are also very similar. Residual patterns formed by (spatially) regressing the (same) regression pattern for EI out of each of these three patterns, shown in Fig. S5 of the supplementary material, are also very similar. The DEI arguably captures the distinction between the 12-yr low-pass filtered and unfiltered ENSO-like variability as well as either of the other indices.

Also included in Fig. 13 is a South Pacific decadal oscillation index (SPDO), defined here as the mirror image of the PDO (i.e., PC1 of SST* in the South Pacific domain poleward of 20°S, smoothed, for purposes of this figure, with a 12-yr Lanczos filter). The similarity between the spatial patterns based on PDO and SPDO attests to the strong equatorial symmetry of the extratropical component of ENSO-like variability. But the stronger correlation between the EI and the PDO than the SPDO (Tables 2 and 3) suggests that the Northern Hemisphere variability dominates the interdecadal variability.

To explore the seasonality of the SST patterns associated with ENSO-like interdecadal variability, we compare, in Fig. 14, SST regression patterns for the

boreal winter months (November–March) and summer months (May–September), using the DEI as an index. For ease of comparison, amplitudes are expressed per unit amplitude of the reference time series, as explained in the caption, rather than as a degrees Celsius per degree Celsius anomaly in the CTI. The patterns observed during the two seasons are almost identical and they are comparable in strength.

b. OLR, SLP, and geopotential height

Figures 3b and 3c contrast the signature of ENSO-like variability in OLR using the EI and DEI as reference time series. The patterns are similar but the low-pass-filtered pattern exhibits a somewhat more complex meridional structure, with anomalies of opposing sign to the north and south of the equator in the equatorial Pacific cold tongue. Given the short length of the OLR record, it is not clear whether the subtle differences between the unfiltered and filtered patterns are statistically significant. In any case, it is clear that the OLR signature of ENSO-like variability is determined to a large degree by the climatology of rainfall itself: the strongest anomalies are observed over the western end of the equatorial dry zone the secondary features tend to trace its outline.

The corresponding SLP regression patterns based on the unfiltered (EI) and filtered (DEI) are shown in the right column of Fig. 5. In the tropics both patterns exhibit the canonical Southern Oscillation signature with a node near or just to the west of the date line at the western end of the equatorial dry zone. As in the patterns for SST* shown in the previous subsection, the extratropical features are strongly accentuated in the 12-yr low-pass-filtered patterns: this is true for both correlation and regression coefficients shown in Fig. 5.
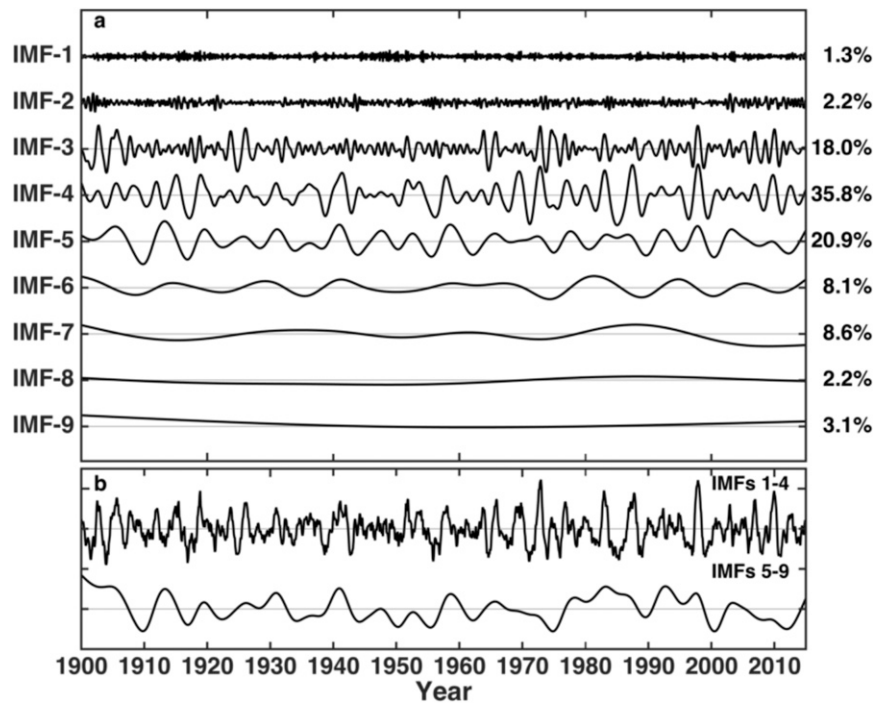
FIG. 9. (a) Individual IMFs of the ENSO index time series EI, with the fraction of the variance of the EI that they explain on the right, scaled so that they sum to 1.0. (b) Sums of IMFs 1–4 and IMFs 5–9. The interval between time scales on the vertical axis is 2.0 and 4.0 standard deviations in (a) and (b), respectively.

The negative center of action over the Gulf of Alaska is especially prominent in the interdecadal ENSO-like variability.

Figure 11 of ZWB gives the impression that the equatorial SLP and wind stress anomalies along the equator are not as strong in the interdecadal variability as in the interannual variability. In contrast, the amplitudes of the SLP anomalies in the unfiltered and 12-yr low-pass-filtered variability in our Fig. 5 are roughly comparable. The difference is attributable to the fact that in ZWB the regression coefficients are expressed in dimensional units per standard deviation of the 12-yr low-pass-filtered time series, whereas in this paper they are expressed in units of hectopascals per degree Celsius of SST anomalies in the cold tongue region.

To appreciate the dynamical significance of the ENSO-related SLP anomalies over the extratropical North Pacific it is useful to view them from a Northern Hemisphere perspective, in combination with upper-level geopotential height anomalies, focusing on the winter months November–March, when they are most strongly coupled with the tropical SST anomalies, as shown in Fig. 15. Consistent with Fig. 5, the SLP anomalies (per degree Celsius of the CTI) are much stronger in the interdecadal variability, as represented

by the DEI, than in the interannual variability, as represented by the EI. Apart from the difference in amplitude, the patterns are similar over the Pacific sector, but not over the hemisphere as a whole. The corresponding pattern in the 500-hPa height field based on the
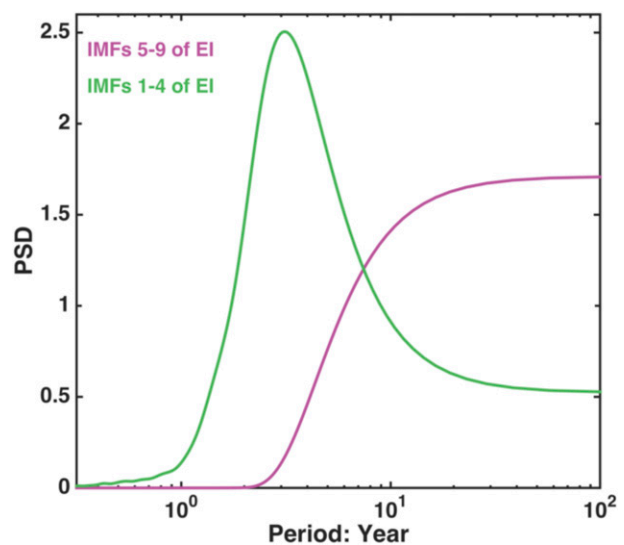

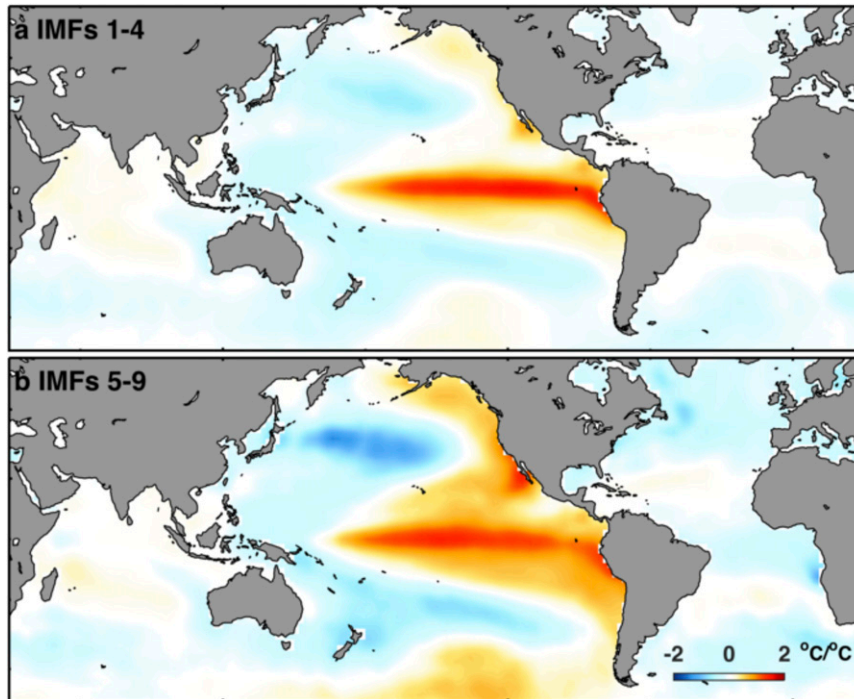FIG. 10. Power spectra of the IMFs 1–4 (green) and IMFs 5–9 (pink).

FIG. 11. Regression coefficients of unfiltered monthly SST* field upon the combination of (a) IMFs 1–4 and (b) IMFs 5–9 of EI, expressed in units of degrees Celsius per degree Celsius of the CTI.

DEI bears a strong resemblance to the Pacific–North American (PNA) pattern (Wallace and Gutzler 1981), one of the dominant modes of internal variability of the Northern Hemisphere wintertime circulation that is present even in atmospheric general circulation models that are not coupled to an interactive ocean [e.g., see Fig. 5 of Lau (1997)]. It corresponds to the least strongly damped mode of barotropic instability of the two-dimensional flow at the jet stream level (Simmons et al. 1983). The corresponding summertime patterns shown in Fig. S6 of the supplementary material are weak and disorganized.

c. OT*

Patterns obtained by regressing the ocean temperature integrated over the topmost 75-m layer upon the EI and the DEI are contrasted in the left panels of Fig. 16. The pattern based on the EI is virtually identical to that based on the PC1 of OT* shown in Fig. 8a. In contrast, the pattern based on the DEI mirrors the corresponding for SST* pattern shown in Fig. 13a, including the anomalies extending into the extratropical North Pacific. The interdecadal pattern is thus suggestive of the behavior of a slab ocean. The corresponding patterns for the 75–700-m layer, shown in the right-hand panels of Fig. 16, are suggestive of enhanced extratropical variability on the interdecadal time scale.

We have also examined the frequency dependence of the three-dimensional structure of the OT* field, as revealed by vertical cross sections for the leading EOF, analogous to those shown in Fig. 7, but using the EI and DEI as reference time series. As shown in Figs. S7 and S8 of the supplementary material, the patterns are qualitatively similar. Although the interdecadal variability in OT is smaller than the interannual variability in an absolute sense, the anomalies in the apparent Rossby wave
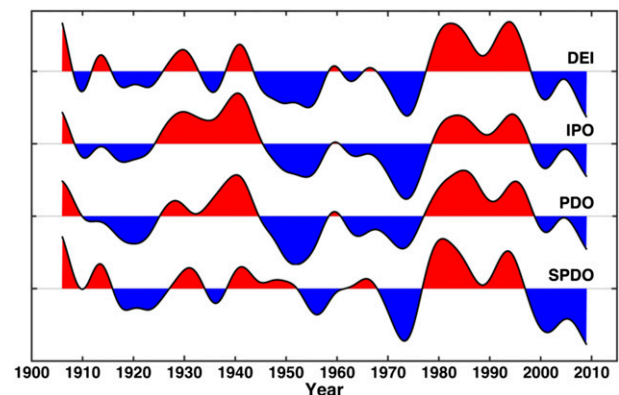

FIG. 12. The 12-yr Lanczos low-pass-filtered PC1 of global SST* (also known as the DEI), the Pacific decadal oscillation (PDO) index, the South Pacific decadal oscillation index (SPDO), and the unfiltered interdecadal Pacific oscillation index (IPO). The scaling is arbitrary.
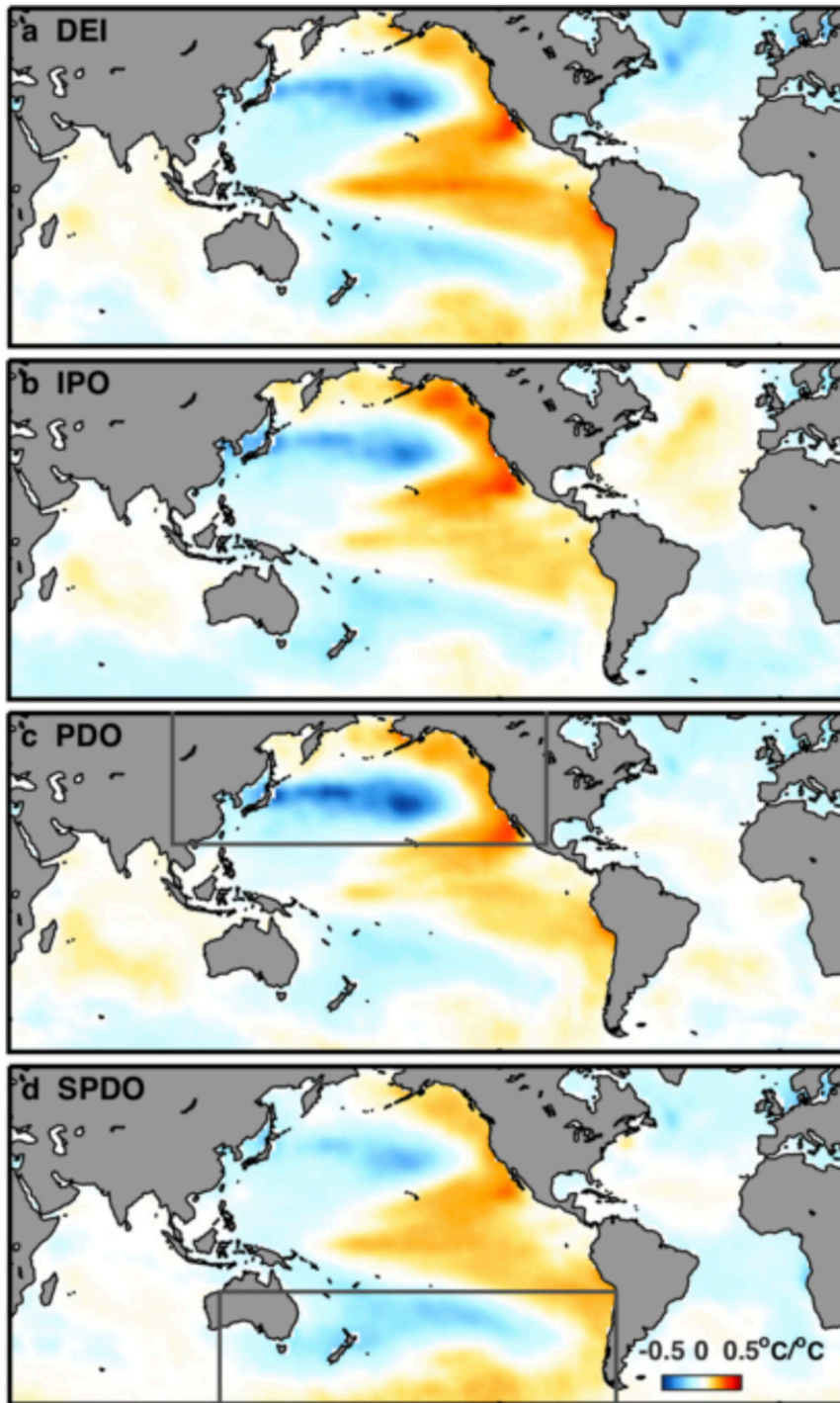
FIG. 13. Regression patterns of unfiltered monthly mean SST* upon the (a) DEI, (b) IPO index, (c) PDO index, and (d) SPDO index, expressed in units of degrees Celsius per degree Celsius of the CTI. The rectangles indicate the domains of the regional EOF analyses upon which the PDO and SPDO are based.
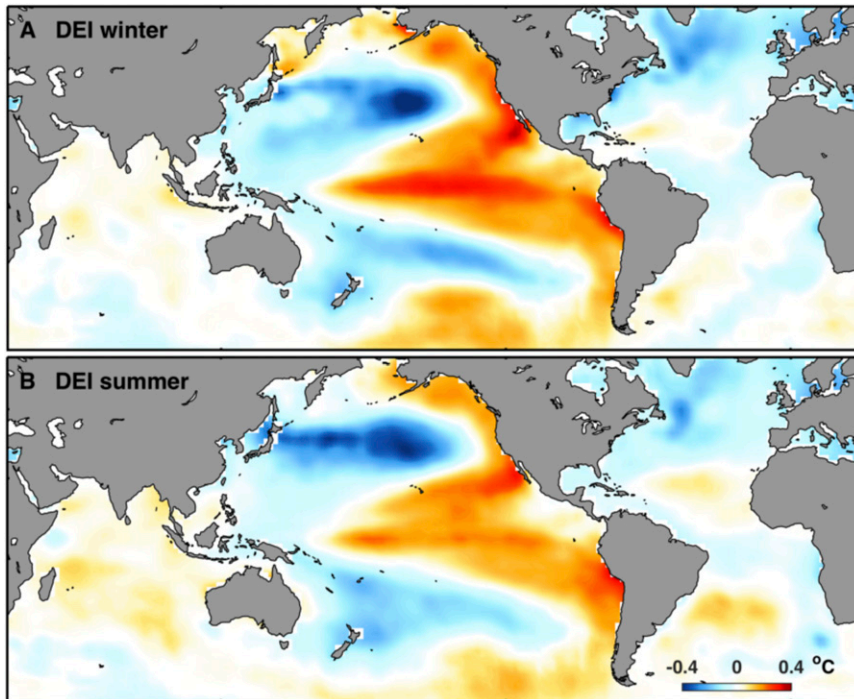
FIG. 14. As in Fig. 13a, but based on (a) means for winter (November–March) and (b) means for summer (May–September). Regression coefficients are expressed in units of degrees Celsius per standard deviation of the DEI.

signature in the western Pacific are accentuated in the interdecadal variability. Consistent with the SST patterns, the DEI signature is wider in the eastern Pacific.

d. Synthesis

Figure 17 shows time series of four indices of ENSO-like interdecadal variability, DEI, low-pass-filtered EEI

(DEEI), SOI*, and TG. Mindful of the lower correlation between TG and the other time series prior to 1950 in the unfiltered data, TG is shown only from 1950 onward. The remarkable degree of agreement indicates that the DEI provides useful information on the interdecadal variability extending back to 1906. The multivariate analysis supports the notion that the interdecadal
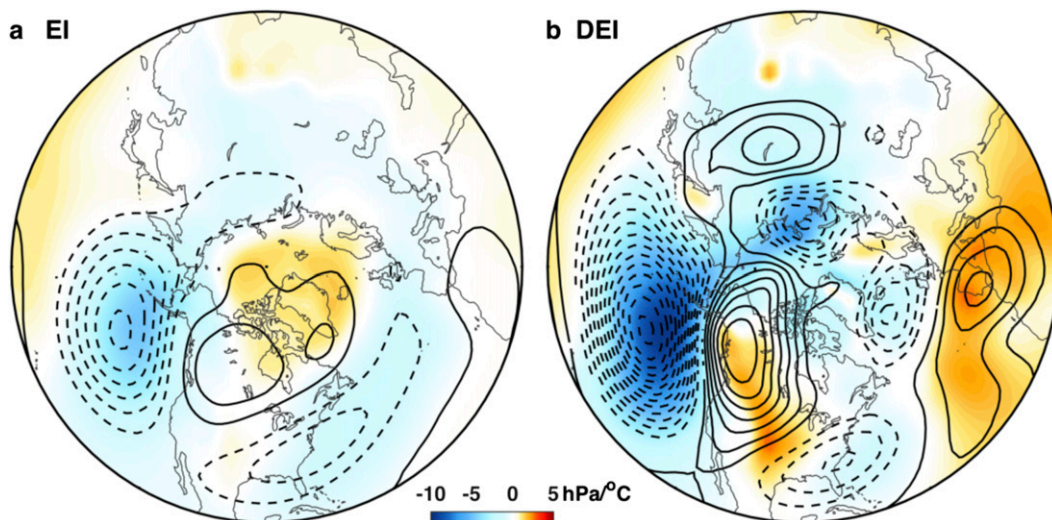

FIG. 15. Wintertime (November–March) SLP (colored shading) and 500-hPa height (contours) regressed upon the (a) EI and (b) DEI, based on data from the 1919/20 winter through the 2013/14 winter. The contour interval for 500-hPa height is $10 \, \text{m} \, (°\text{C})^{-1}$ of the CTI.
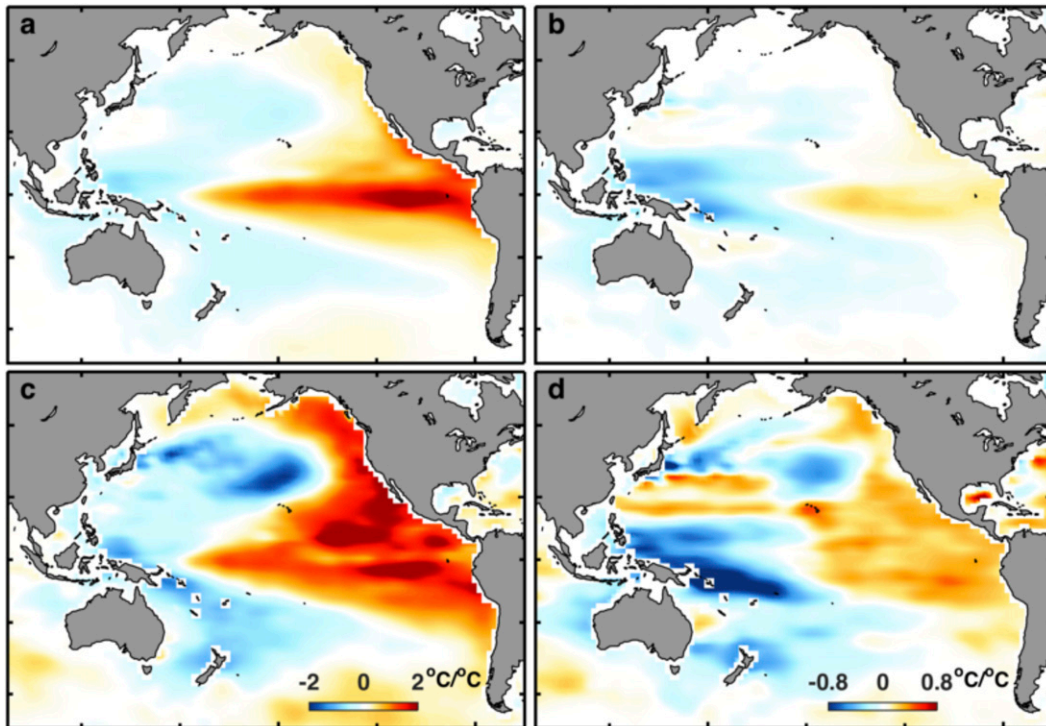
FIG. 16. Regression patterns of the vertically integrated OT* in the (left) 0–75-m and (right) the 75–700-m layer based on the (a),(b) EI and (c),(d) DEI, expressed in units of degrees Celsius per degree Celsius of the CTI.

shifts that occurred in the late 1970s and the late 1990s were more prominent than the earlier features in the record. Hence it is questionable whether ENSO-like interdecadal variability is inherently oscillatory, as argued by Minobe (1997) and as implied by many of the terms that are used to characterize it.

The Lanczos-smoothed time series shown in this section end in 2007. Figure 18 shows annual mean SST pattern for the years 2011–13, 2014, and early 2015. The patterns for 2011–13 were quite typical of the recent epoch of strong trade winds. By 2014 SST along the northern part of the Pacific rim had warmed substantially and in early 2015 SST was well above normal in the eastern Pacific from Baja California northward, suggestive of a regime shift, but whether it will be sustained remains to be seen.

5. Discussion

In the observations, ENSO-like variability across the full range of frequencies is characterized by equatorial SST Pacific anomalies extending from ~165°E to the coast of South America (Figs. 2a,b), a dipole pattern of tropical rainfall anomalies whose eastern pole is centered at the western end of the climatological-mean equatorial Pacific dry zone

(Figs. 3a,b), and the canonical Southern Oscillation SLP signature with the node at the western end of the dry zone (Fig. 5a).

Interannual ENSO-like variability in the SST field tends to be focused within the equatorial belt, whereas interdecadal ENSO-like variability in the SST field includes subtropical and extratropical signatures (cf. Figs. 11a and 11b). The interdecadal variability in the SLP field features a more prominent center of action over the Gulf of Alaska, which resembles the SLP
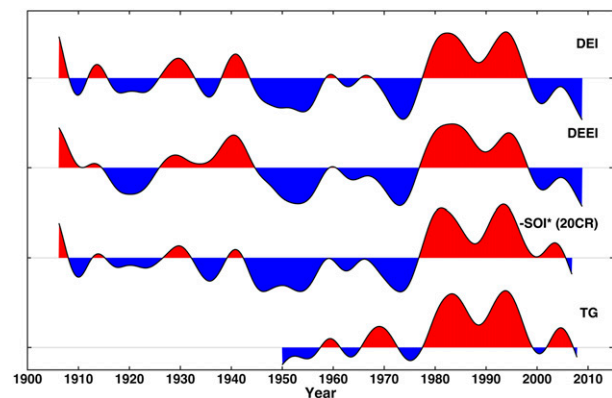

FIG. 17. The 12-yr Lanczos low-pass–filtered EI (i.e., the DEI), DEEI, SOI*, and TG. Scaling is arbitrary.
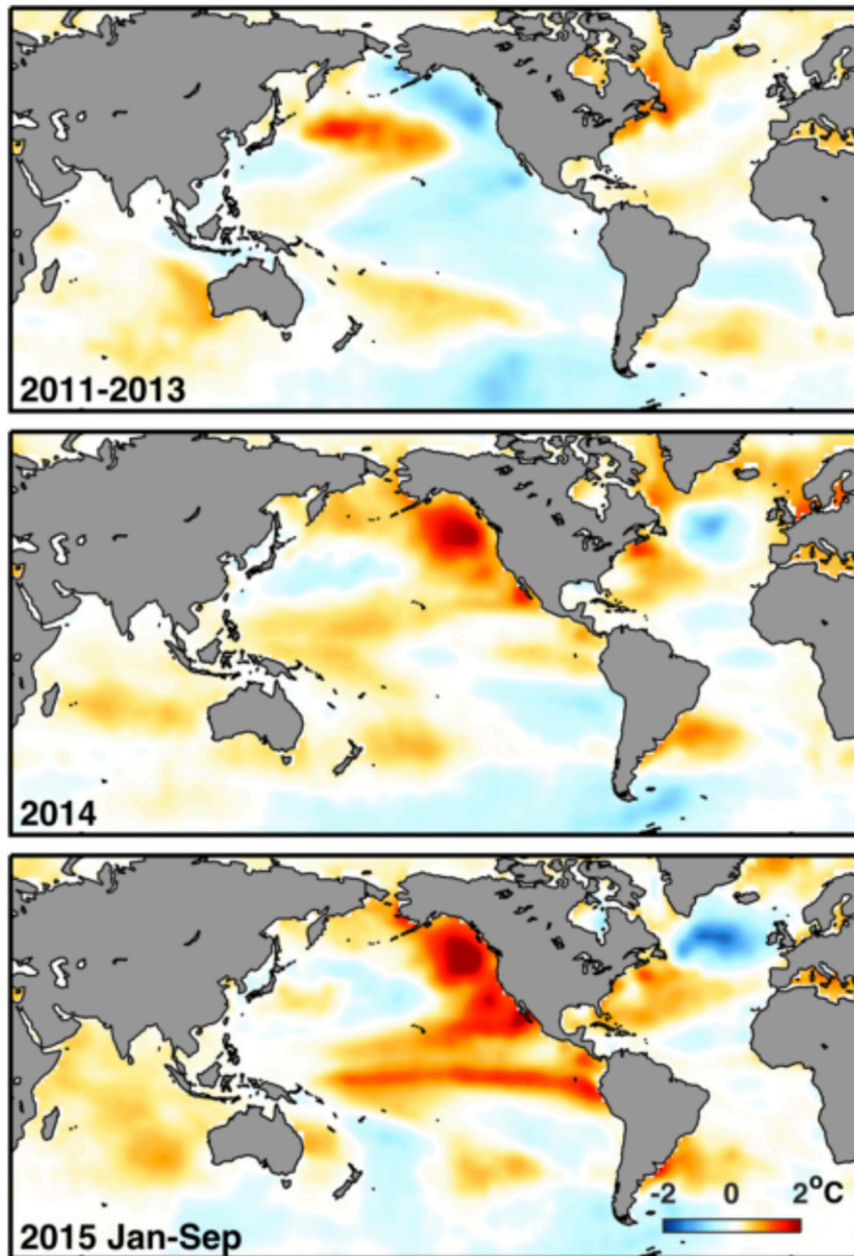
FIG. 18. Annual mean SST anomalies for calendar years 2011–13, 2014, and for January–September 2015 relative to the 1983–2014 climatology.

signature of the PNA pattern. That the distinctive tropical "Southern Oscillation signature" is prominent in both the interannual and interdecadal variability indicates that Bjerknes feedback is operative on both time scales.

The pattern of interdecadal ENSO-like SST variability and subsurface (0–75 m) ocean temperature anomalies over the North Pacific (Figs. 11b, 13, and 16c) resembles the response to the PNA pattern, as conveyed by the anomalous latent sensible heat fluxes at the air–sea interface (Wallace et al.1990, their Fig. 1). The PNA signature is only observed during the boreal winter (Fig. S6), but the subsurface ocean temperature anomalies persist year-round (Fig. 14).

By virtue of its special relationship to the climatological mean Pacific jet stream, as explained in Simmons et al. (1983), the PNA pattern exhibits large variability in its own right, irrespective of its interaction with the ocean. But just how the ENSO-like and PNA-like variability interact—whether the PNA-like variability in

the extratropical circulation is stochastically forced by the ENSO cycle or whether it is capable of forcing a red noise continuum of ENSO-like variability even in the absence of the ENSO cycle, as suggested by the numerical experiments of Dommenget and Latif (2008)—remains to be determined.

That the tropical–extratropical coupling is much stronger on the interdecadal time scale than on the interannual time scale does not necessarily imply the prevalence of different or frequency-dependent coupling mechanisms: it could simply be a consequence of the fact that the effective sample size for the correlation and regression coefficients increases in proportion to the time scale. In the presence of non-ENSO-like noise, in the variability of the PNA pattern, it is reasonable to expect that the tropical–extratropical coupling should be more clearly apparent on the interdecadal time scale.

The analysis presented in this paper provides a comprehensive and dynamically consistent documentation of ENSO-like variability in the coupled atmosphere–ocean system extending back to 1950 and a somewhat more complete partial description of it than the one in ZWB extending back to 1900. Our analysis confirms the "regime shifts" around 1925, 1942, and 1977 identified by ZWB and the subsequent shift in 1998, but the interdecadal variability does not appear to be oscillatory in the sense of possessing a spectral peak in the frequency domain that would confer some degree of long-range predictability. The DEI, the PDO, and the IPO indices are derived using quite different analysis protocols, but it is clear from Fig. 12 that they all yield quite similar representations of the low-frequency variability.

REFERENCES

Battisti, D. S., and A. C. Hirst, 1989: Interannual variability in the tropical atmosphere–ocean model: Influence of the basic state, ocean geometry and nonlinearity. *J. Atmos. Sci.*, **46**, 1687–1712, doi:10.1175/1520-0469(1989)046<1687:IVIATA>2.0.CO;2.

Bjerknes, J., 1969: Atmospheric teleconnections from the equatorial Pacific. *Mon. Wea. Rev.*, **97**, 163–172, doi:10.1175/1520-0493(1969)097<0163:ATFTEP>2.3.CO;2.

——, 1972: Large-scale atmospheric response to the 1964–65 Pacific equatorial warming. *J. Phys. Oceanogr.*, **2**, 212–217, doi:10.1175/1520-0485(1972)002<0212:LSARTT>2.0.CO;2.

Cane, M. A., and S. E. Zebiak, 1985: A theory for El Niño and the Southern Oscillation. *Science*, **228**, 1085–1087, doi:10.1126/science.228.4703.1085.

Clement, A., P. DiNezio, and C. Deser, 2011: Rethinking the ocean's role in the Southern Oscillation. *J. Climate*, **24**, 4056–4072, doi:10.1175/2011JCLI3973.1.

Compo, G. P., and Coauthors, 2011: The Twentieth Century Reanalysis Project. *Quart. J. Roy. Meteor. Soc.*, **137**, 1–28, doi:10.1002/qj.776.

Deser, C., and J. M. Wallace, 1990: Large-scale atmospheric circulation features of warm and cold episodes in the tropical Pacific. *J. Climate*, **3**, 1254–1281, doi:10.1175/1520-0442(1990)003<1254:LSACFO>2.0.CO;2.

Dommenget, D., 2010: The slab ocean El Niño. *Geophys. Res. Lett.*, **37**, L20701, doi:10.1029/2010GL044888.

——, and M. Latif, 2008: Generation of hyper climate modes. *Geophys. Res. Lett.*, **35**, L02706, doi:10.1029/2007GL031087.

Folland, C. K., D. E. Parker, A. Colman, and R. Washington, 1999: Large scale modes of ocean surface temperature since the late nineteenth century. *Beyond El Niño: Decadal and Interdecadal Climate Variability*, A. Navarra, Ed., Springer-Verlag, 73–102, doi:10.1007/978-3-642-58369-8_4.

Garreaud, R. D., and D. S. Battisti, 1999: Interannual (ENSO) and interdecadal (ENSO-like) variability in the Southern Hemisphere tropospheric circulation. *J. Climate*, **12**, 2113–2123, doi:10.1175/1520-0442(1999)012<2113:IEAIEL>2.0.CO;2.

Graham, N. E., 1994: Decadal-scale climate variability in the 1970s and 1980s: Observations and model results. *Climate Dyn.*, **10**, 135–162, doi:10.1007/BF00210626.

Heddinghaus, T. R., and A. F. Krueger, 1981: Annual and interannual variations in outgoing longwave radiation over the tropics. *Mon. Wea. Rev.*, **109**, 1208–1218, doi:10.1175/1520-0493(1981)109<1208:AAIVIO>2.0.CO;2.

Huang, N. E., and Coauthors, 1998: The empirical mode decomposition and the Hilbert spectrum for nonlinear and nonstationary time series analysis. *Proc. Roy. Soc. London*, **454**, 903–995, doi:10.1098/rspa.1998.0193.

Ishii, M., and M. Kimoto, 2009: Reevaluation of historical ocean heat content variations with time-varying XBT and MBT depth bias corrections. *J. Oceanogr.*, **65**, 287–299, doi:10.1007/s10872-009-0027-7.

Kitoh, A., T. Motoi, and H. Koide, 1999: SST variability and its mechanism in a coupled atmosphere–mixed layer ocean model. *J. Climate*, **12**, 1221–1239, doi:10.1175/1520-0442(1999)012<1221:SVAIMI>2.0.CO;2.

Lau, N.-C., 1997: Interactions between global SST anomalies and the midlatitude atmospheric circulation. *Bull. Amer. Meteor. Soc.*, **78**, 21–33, doi:10.1175/1520-0477(1997)078<0021:IBGSAA>2.0.CO;2.

——, S. G. H. Philander, and M. J. Nath, 1992: Simulation of ENSO-like phenomena with a low-resolution coupled GCM of the global ocean and atmosphere. *J. Climate*, **5**, 284–307, doi:10.1175/1520-0442(1992)005<0284:SOELPW>2.0.CO;2.

Liebmann, B., and C. A. Smith, 1996: Description of a complete (interpolated) outgoing longwave radiation dataset. *Bull. Amer. Meteor. Soc.*, **77**, 1275–1277.

Lombard, A., A. Cazenave, P.-Y. Le Traon, and M. Ishii, 2005: Contribution of thermal expansion to present-day sea-level change revisited. *Global Planet. Change*, **47**, 1–16, doi:10.1016/j.gloplacha.2004.11.016.

Mantua, N. J., S. R. Hare, Y. Zhang, J. M. Wallace, and R. C. Francis, 1997: A Pacific interdecadal climate oscillation with impacts on salmon production. *Bull. Amer. Meteor. Soc.*, **78**, 1069–1079, doi:10.1175/1520-0477(1997)078<1069:APICOW>2.0.CO;2.

Minobe, S., 1997: A 50–70 year climatic oscillation over the North Pacific and North America. *Geophys. Res. Lett.*, **24**, 683–686, doi:10.1029/97GL00504.

Nerem, R. S., K. E. Rachlin, and B. D. Beckley, 1997: Characterization of global mean sea level variations observed by TOPEX/Poseidon using empirical orthogonal functions. *Surv. Geophys.*, **18**, 293–302, doi:10.1023/A:1006596211926.

Newman, M., 2007: Interannual to decadal predictability of tropical and North Pacific sea surface temperatures. *J. Climate*, **20**, 2333–2356, doi:10.1175/JCLI4165.1.

Nitta, T., and S. Yamada, 1989: Recent warming of tropical sea surface temperature and its relationship to the Northern Hemisphere circulation. *J. Meteor. Soc. Japan*, **67**, 375–383.

Penland, C., and P. D. Sardeshmukh, 1995: The optimal growth of tropical sea surface temperature anomalies. *J. Climate*, **8**, 1999–2024, doi:10.1175/1520-0442(1995)008<1999:TOGOTS>2.0.CO;2.

Rasmusson, E. M., and T. H. Carpenter, 1982: Variations in the tropical sea surface temperature and surface wind fields associated with the Southern Oscillation–El Niño. *Mon. Wea. Rev.*, **110**, 354–384, doi:10.1175/1520-0493(1982)110<0354:VITSST>2.0.CO;2.

Roemmich, D., and J. Gilson, 2011: The global ocean imprint of ENSO. *Geophys. Res. Lett.*, **38**, L13606, doi:10.1029/2011GL047992.

Simmons, A. J., J. M. Wallace, and G. W. Branstator, 1983: Barotropic wave propagation and instability, and atmospheric teleconnection patterns. *J. Atmos. Sci.*, **40**, 1363–1392, doi:10.1175/1520-0469(1983)040<1363:BWPAIA>2.0.CO;2.

Trenberth, K. E., 1990: Recent observed interdecadal climate changes in the Northern Hemisphere. *Bull. Amer. Meteor. Soc.*, **71**, 988–993, doi:10.1175/1520-0477(1990)071<0988:ROICCI>2.0.CO;2.

——, and D. J. Shea, 1987: On the evolution of the Southern Oscillation. *Mon. Wea. Rev.*, **115**, 3078–3096, doi:10.1175/1520-0493(1987)115<3078:OTEOTS>2.0.CO;2.

——, and J. W. Hurrell, 1994: Decadal atmosphere–ocean variations in the Pacific. *Climate Dyn.*, **9**, 303–319, doi:10.1007/BF00204745.

——, and T. J. Hoar, 1997: El Niño and climate change. *Geophys. Res. Lett.*, **24**, 3057–3060, doi:10.1029/97GL03092.

——, and D. J. Shea, 2006: Atlantic hurricanes and natural variability in 2005. *Geophys. Res. Lett.*, **33**, L12704, doi:10.1029/2006GL026894.

Troup, A. J., 1965: The Southern Oscillation. *Quart. J. Roy. Meteor. Soc.*, **91**, 490–506, doi:10.1002/qj.49709139009.

Vimont, D. J., D. S. Battisti, and A. C. Hirst, 2002: Pacific interannual and interdecadal equatorial variability in a 1000-yr simulation of the CSIRO coupled general circulation model. *J. Climate*, **15**, 160–178, doi:10.1175/1520-0442(2002)015<0160:PIAIEV>2.0.CO;2.

Wallace, J. M., and D. S. Gutzler, 1981: Teleconnections in the geopotential height field during the Northern Hemisphere winter season. *Mon. Wea. Rev.*, **109**, 784–812, doi:10.1175/1520-0493(1981)109<0784:TITGHF>2.0.CO;2.

——, C. Smith, and Q. Jiang, 1990: Spatial patterns of atmosphere–ocean interaction in the northern winter. *J. Climate*, **3**, 990–998, doi:10.1175/1520-0442(1990)003<0990:SPOAOI>2.0.CO;2.

Wu, Z., and N. E. Huang, 2004: A study of the characteristics of white noise using the empirical mode decomposition method. *Proc. Roy. Soc. London*, **460A**, 1597–1611, doi:10.1098/rspa.2003.1221.

Zebiak, S. E., and M. A. Cane, 1987: A model El Niño–Southern Oscillation. *Mon. Wea. Rev.*, **115**, 2262–2278, doi:10.1175/1520-0493(1987)115<2262:AMENO>2.0.CO;2.

Zhang, W., J. Li, and X. Zhao, 2010: Sea surface temperature cooling mode in the Pacific cold tongue. *J. Geophys. Res.*, **115**, C12042, doi:10.1029/2010JC006501.

Zhang, Y., J. M. Wallace, and D. S. Battisti, 1997: ENSO-like interdecadal variability: 1900–93. *J. Climate*, **10**, 1004–1020, doi:10.1175/1520-0442(1997)010<1004:ELIV>2.0.CO;2.